Supplement of Atmos. Chem. Phys., 24, 3043–3063, 2024
https://doi.org/10.5194/acp-24-3043-2024-supplement

Atmospheric Chemistry and Physics
Open Access
EGU

Supplement of

Morphological and optical properties of carbonaceous aerosol particles from ship emissions and biomass burning during a summer cruise measurement in the South China Sea

Cuizhi Sun et al.

Correspondence to: Shengzhen Zhou (zhoushzh3@mail.sysu.edu.cn) and Jun Zhao (zhaojun23@mail.sysu.edu.cn)

S1. Calculation of the cut size diameter of the TEM sampler

A single-stage cascade impactor, equipped with a jet nozzle of 0.3 mm in diameter, was used for single-particle sampling. The Stokes number is defined in Eqs. (1)–(2) (Marple and Olson, 2011). The cut-size diameter, which is defined as the diameter corresponding to a 50% collection efficiency, can be derived using Eq. (3).

$$Stk = \frac{\rho_p C_c d_p^2 U}{9\eta W} \quad (1)$$

$$U = \frac{Q}{\pi(\frac{W}{2})^2} \quad (2)$$

$$d_{p_{50}} = \sqrt{Stk_{50}}\sqrt{\frac{9\eta\pi W^3}{4\rho_p C_c Q}} \quad (3)$$

where Stk is Stokes number, and the square root of the Stk corresponding to 50% collection efficiency ($\sqrt{Stk_{50}}$) is 0.47 assumed a jet Reynolds number of 3000; ρ_p is particle density assumed as 1.5 g cm^{-3}; C_c is Cunningham's slip correction factor, approximately 1; η is air (or gas) viscosity, 1.8134×10^{-5} Pa·s at 293 K, a constant under normal atmospheric condition. U represents the average air (or gas) velocity at the nozzle exit; Q is the volumetric flow rate through the nozzle and is equal to 1 L min^{-1}; W is the nozzle diameter and is 0.3 mm; $d_{p_{50}}$ is the cut point particle diameter at the 50% collection efficiency.

S2. Single particle analysis using the ImageJ's plugin

Figure S1 shows examples of TEM images using the software program ImageJ for single-particle analysis. Figure S1a is captured before beam focus, which is subsequently used for single-particle analysis in Fig. S1b. However, particles No. 2 and No. 13 (indicated by the red arrow) were manually excluded from the statistical analysis due to overcounting. In Fig. S1c, volatile components were vaporized after beam focus, leaving nonvolatile compositions such as BC residual on the substrate (e.g., particles indicated by the blue arrow). The outline of BC aggregates was extracted using ImageJ's Frac Lac plugin (deep ImageJ) for fractal dimension calculation, which is based on the box counting method, for example, the image inside the blue rectangle on the lower right corner of Fig. S1c.

In the box counting method, the theoretical basis for D_f calculation is following Eq. (4).

$$D_f = \frac{\ln N}{\ln \varepsilon} \quad (4)$$

where D_f is fractal dimension, N is the number of the primary monomers of the aggregate, ε is the scale factor relating to the radius of gyration, the average radius of the monomer and fractal prefactor (Sorensen and Roberts, 1997).

Lacunarity measures gap and heterogeneity to complement fractal dimensions in describing complexity. It uses box mass instead of box count as mentioned in the Fraclac guidelines in the ImageJ software. The Fraclac calculates L from the pixel distribution in the TEM binary image.

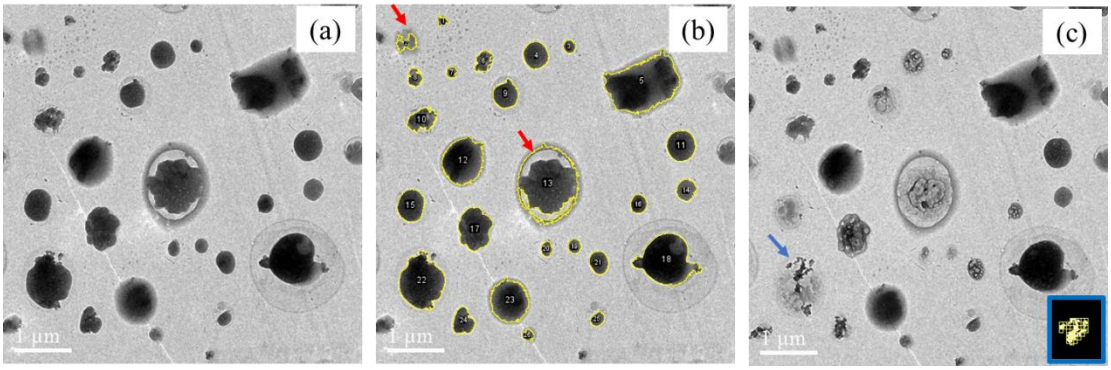

Fig. S1. Example images of the single-particle analysis using ImageJ's plugin: **(a)** Before beam focus in the TEM image, and **(b)** particles marked with numbers in yellow using ImageJ, and **(c)** after beam focus in the TEM image.

S3. Meteorological data for single particle sampling during navigation and stop

The time series of ship heading, relative wind direction (RWD), and relative wind speed (RWS) with a time resolution of 3 s in the South China Sea (SCS) during the campaign (5 May–9 June 2021) is shown in Fig. S2. The RWD and RWS varied considerably and frequently due to the operational starts and stops (halts) of the ship for other tasks. The 10-min average of RWD and RWS data were determined based on vector calculations. Detailed meteorological data, encompassing the 10-min average for single-particle sampling during navigation and stop, are listed in Table S1. The sampling location for single-particle sampling is shown in Fig. S3.

Note that the samples collected during navigation were free from interference from the ship's own emission due to high relative wind speeds (>5 m s^{-1}) and appropriate relative wind directions (0°–80°, 280°–360°). Samples collected with wind speeds below 5 m s^{-1} or at relative wind direction in the range

of 80°–280° were air masses mixed with the own ship emissions.

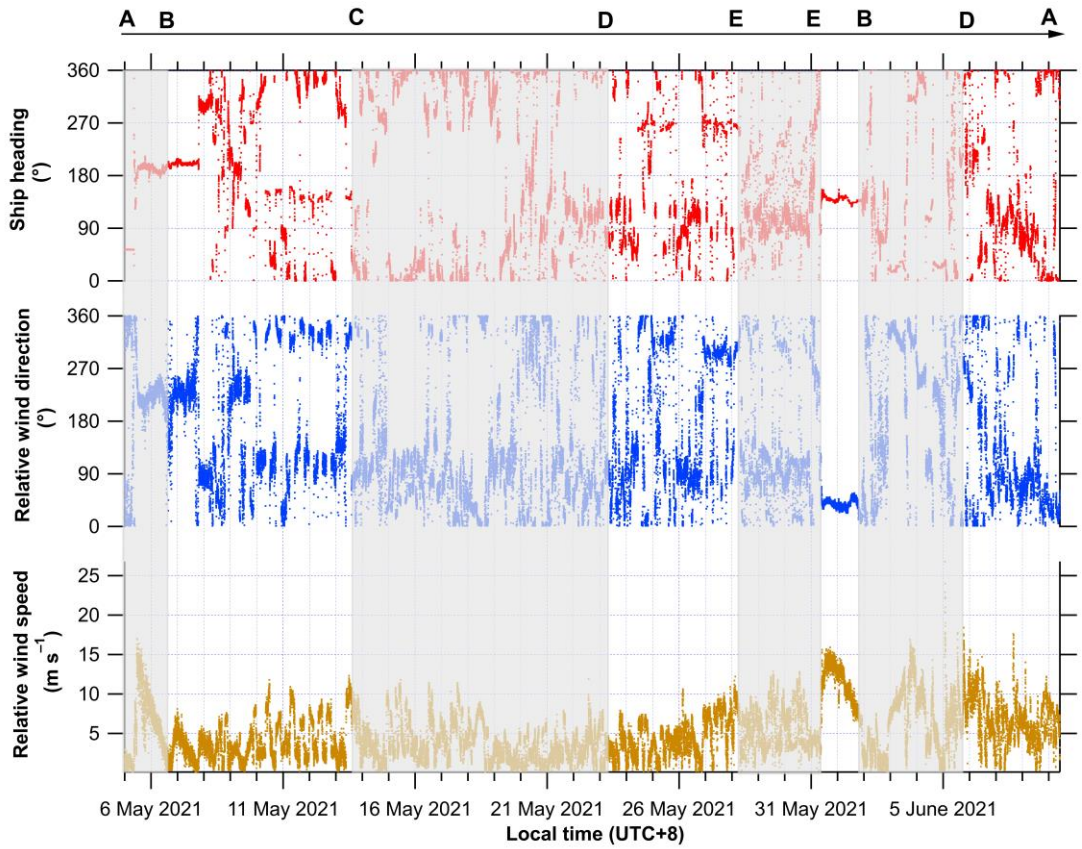

Fig. S2. Time series of ship heading, relative wind direction (RWD), and relative wind speed (RWS) during the campaign in the South China Sea (SCS). The shaded and unshaded areas sequentially indicate the cruise routes from AB, B→C, C→ D, D→E, E (ship stop), EB, B→D, and D→A, as marked in Fig. 1 in the main text. The routes AB and EB are non-stop cruise, and other routes are with some ship stops.

Table S1. Meteorological data on the 10-min average single particle sampling during navigation and stop.

Serial number	Sampling start time	P (hPa)	RH (%)	S.R. (W m^{-2})	Temp. (°C)	RWS* (m s^{-1})	RWD* (°)
N1	11:18:00 10/5/2021	1008.3 ± 0.0	81.0 ± 0.7	961.9 ± 42.4	29.7 ± 0.0	10.5 ± 0.6	341.7 ± 50.7
N2	08:24:00 11/5/2021	1007.9 ± 0.0	83.3 ± 0.5	491.6 ± 10.1	28.9 ± 0.1	9.8 ± 0.5	320.2 ± 46.7
N3	19:00:00 11/5/2021	1006.6 ± 0.1	75.5 ± 0.5	NaN	29.7 ± 0.0	6.4 ± 0.8	336.1 ± 21.1
N4	08:13:00 12/5/2021	1007.5 ± 0.1	78.8 ± 0.6	474.5 ± 32.9	29.4 ± 0.1	7.0 ± 0.4	327.7 ± 53.1
N5	19:15:00 15/5/2021	1006.6 ± 0.0	77.8 ± 1.9	NaN	30.2 ± 0.1	6.2 ± 0.7	60.1 ± 37.2
N6	12:35:00 16/5/2021	1007.5 ± 0.0	76.9 ± 0.7	989.8 ± 13.2	29.8 ± 0.0	10.8 ± 0.7	340.3 ± 59.0

N7	14:40:00 17/5/2021	1006.6 ± 0.0	72.2 ± 0.9	758.7 ± 7.7	30.0 ± 0.0	10.0 ± 0.6	16.9 ± 47.7
N8	08:47:00 18/5/2021	1009.3 ± 0.0	79.3 ± 0.5	647.1 ± 68.5	30.1 ± 0.0	7.3 ± 0.5	12.3 ± 59.7
N9	18:10:00 18/5/2021	1007.0 ± 0.0	75.8 ± 0.4	28.5 ± 6.1	30.7 ± 0.0	5.3 ± 0.4	14.2 ± 50.4
N10	16:16:00 21/5/2021	1006.2 ± 0.1	74.0 ± 0.5	244.8 ± 62.2	30.2 ± 0.0	6.0 ± 1.2	16.8 ± 29.5
N11	15:32:00 22/5/2021	1005.3 ± 0.0	82.1 ± 0.7	551.3 ± 140.5	28.5 ± 0.1	6.3 ± 1.0	57.4 ± 19.6
N12	08:55:00 27/5/2021	1009.2 ± 0.0	76.1 ± 0.7	666.6 ± 16.4	29.8 ± 0.1	7.0 ± 0.4	291.8 ± 45.9
N13	18:07:00 1/6/2021	1004.7 ± 0.0	76.1 ± 0.3	78.6 ± 14.6	30.3 ± 0.0	8.0 ± 0.5	40.0 ± 45.2
N14	10:50:00 3/6/2021	1005.4 ± 0.1	77.9 ± 0.7	151.9 ± 6.7	30.1 ± 0.0	10.1 ± 0.5	313.2 ± 61.3
N15	10:18:00 8/6/2021	1008.8 ± 0.0	86.2 ± 0.4	259.7 ± 40.5	28.4 ± 0.1	5.1 ± 0.7	58.6 ± 19.7
S1	14:36:00 9/5/2021	1007.2 ± 0.0	74.6 ± 0.5	739.4 ± 164.0	29.4 ± 0.1	1.8 ± 0.7	242.4 ± 62.3
S2	15:30:00 9/5/2021	1006.6 ± 0.1	75.3 ± 0.8	686.9 ± 32.3	29.5 ± 0.2	3.0 ± 0.6	238.5 ± 42.3
S3	09:07:00 13/5/2021	1006.6 ± 0.0	77.1 ± 0.6	709.6 ± 12.6	30.4 ± 0.0	0.1 ± 1.3	222.1 ± 32.9
S4	19:15:00 13/5/2021	1005.8 ± 0.0	65.0 ± 1.4	NaN**	30.4 ± 0.1	5.5 ± 2.1	95.9 ± 67.1
S5	10:50:00 14/5/2021	1006.9 ± 0.0	75.4 ± 0.5	932.7 ± 4.1	30.9 ± 0.1	2.4 ± 0.7	193.3 ± 38.7
S6	21:50:00 16/5/2021	1008.3 ± 0.1	77.3 ± 0.8	NaN	29.8 ± 0.1	3.7 ± 0.5	68.3 ± 48.3
S7	21:12:00 18/5/2021	1008.0 ± 0.0	77.0 ± 0.0	NaN	30.5 ± 0.0	0.5 ± 0.4	128.1 ± 51.4
S8	08:42:00 19/5/2021	1008.2 ± 0.0	74.8 ± 0.6	661.4 ± 6.3	31.0 ± 0.1	2.1 ± 0.6	123.0 ± 32.5
S9	18:00:00 20/5/2021	1007.7 ± 0.1	68.5 ± 0.5	54.4 ± 8.6	31.6 ± 0.1	0.3 ± 0.3	109.5 ± 40.4
S10	08:40:00 22/5/2021	1008.0 ± 0.1	73.8 ± 0.6	278.1 ± 136.2	30.2 ± 0.1	1.3 ± 0.3	43.1 ± 66.1
S11	08:39:00 23/5/2021	1007.6 ± 0.1	74.9 ± 0.7	646.7 ± 9.9	30.1 ± 0.1	3.2 ± 0.6	83.0 ± 61.8
S12	20:43:00 23/5/2021	1008.6 ± 0.0	80.4 ± 0.7	NaN	29.1 ± 0.1	3.6 ± 0.6	91.5 ± 69.4
S13	08:01:00 24/5/2021	1009.3 ± 0.0	74.9 ± 0.3	526.1 ± 10.5	30.3 ± 0.1	2.5 ± 0.5	133.4 ± 43.6
S14	16:03:00 24/5/2021	1007.1 ± 0.0	75.7 ± 0.8	94.5 ± 4.9	30.4 ± 0.1	2.4 ± 0.7	76.9 ± 48.1
S15	09:21:00 25/5/2021	1010.1 ± 0.0	77.6 ± 0.5	734.1 ± 86.0	29.8 ± 0.1	4.7 ± 0.5	317.3 ± 47.0
S16	22:11:00 30/5/2021	1002.9 ± 0.1	96.0 ± 0.0	NaN	27.3 ± 0.0	2.0 ± 0.3	108.9 ± 68.7
S17	09:10:00 2/6/2021	1007.2 ± 0.0	78.5 ± 0.5	675.9 ± 17.1	29.8 ± 0.1	3.1 ± 0.4	17.6 ± 42.1
S18	18:23:00 5/6/2021	1003.0 ± 0.1	83.8 ± 0.4	2.3 ± 0.5	29.0 ± 0.1	11.8 ± 0.9	279.0 ± 36.0
S19	08:45:00 7/6/2021	1006.7 ± 0.1	86.3 ± 0.9	110.9 ± 36.6	27.8 ± 0.1	4.1 ± 3.2	105.5 ± 45.3

* The relative wind direction and wind speed are 10-min vector average. ** NaN indicates no data.

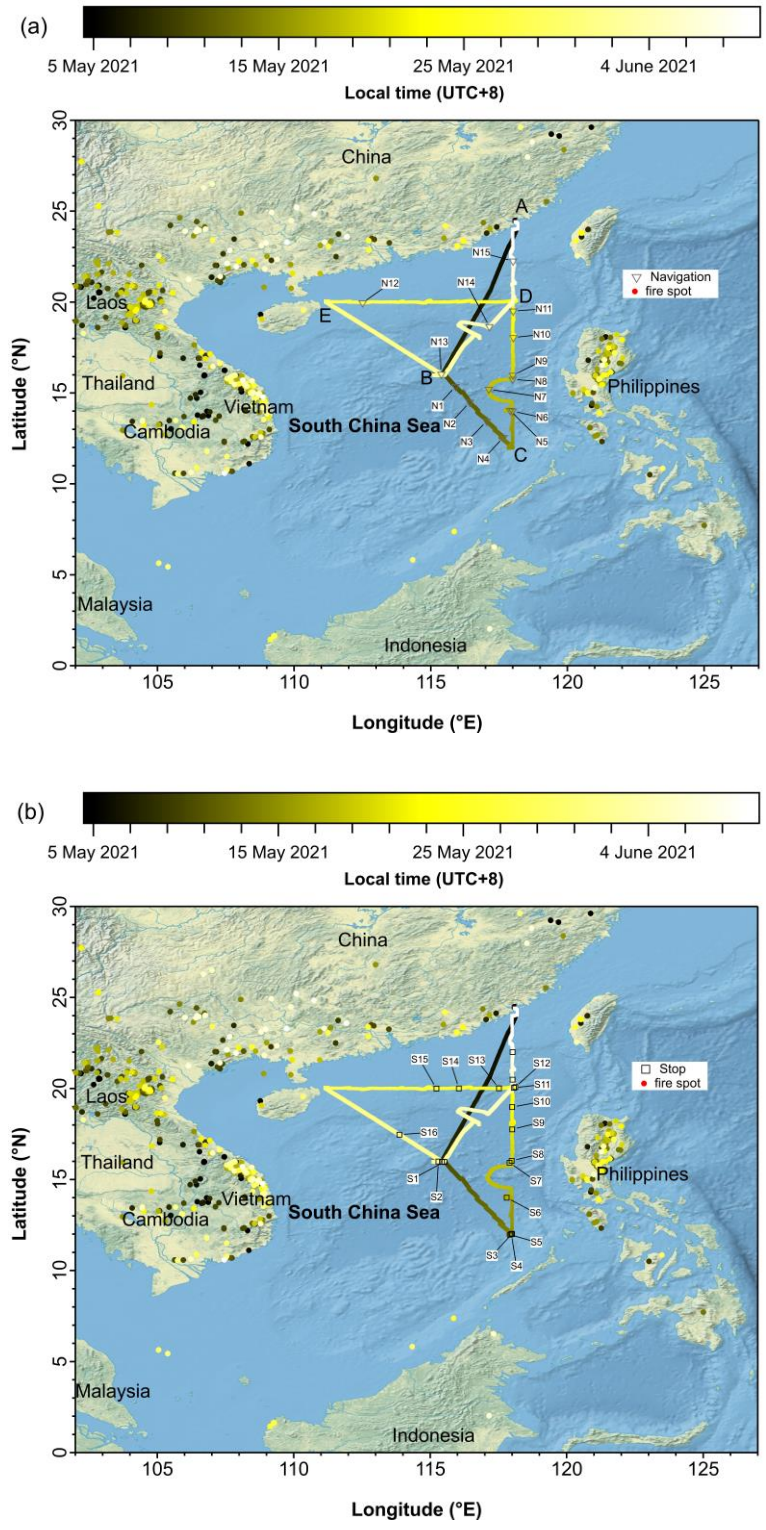

Fig. S3. Map of the ship route in the South China Sea during the campaign. The open triangles in **(a)** and squares in **(b)** indicate the single particle sampling location, collected during navigation and stop. The samples marked in N1–15 for navigation sampling and S1–19 for stop sampling in serial. The solid circles indicate the fire spots with a confidence level greater than 80% using MODIS satellite data.

S4. AAE calculation

The long-range biomass burning transport affects the air mass in the South China Sea (SCS). Two methods were used to obtain the hourly absorption Ångström exponent (AAE) values from the AE33 measurements. Figure S4a shows an example of the AAE calculation for a ship plume at 18:00:00 LT on 5 May 2021. Figure S4b demonstrates the linear relationship between the AAE values obtained from all wavelengths and those obtained from a pair of wavelengths at 470 and 950 nm. The fitting results indicate that AAE (all wavelengths) was lower than AAE (470, 950 nm) with a fitting slope of 0.78 and a determination coefficient (R^2) of 0.98.

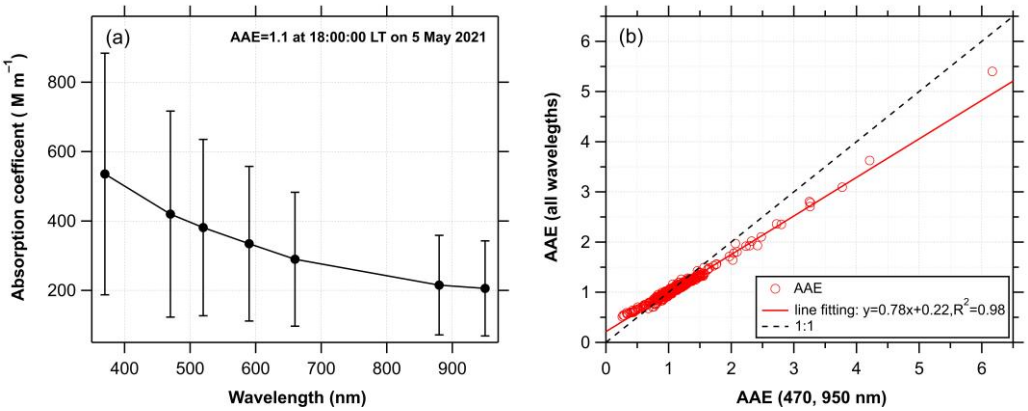

Fig. S4. (a) A ship plume at 18:00:00 LT on 5 May 2021, for the wavelength-dependent absorption Ångström exponent (AAE) based on the hourly averaged data, and **(b)** AAE obtained from all the wavelengths vs. the AAE obtained from two wavelengths at 470 and 950 nm based on hourly averaged data during the campaign.

S5. Typhoon 202103 (CHOI-WAN)

Typhoon 202103 (CHOI-WAN) was born at 18:00:00 UTC on 30 May 2021, and dead at 06:00:00 UTC on 5 June 2021. We met this typhoon during our cruise measurement. Figure S5 shows the best track of the map and central pressure chart. Basic information is available online (http://agora.ex.nii.ac.jp/digital-typhoon/summary/wnp/s/202103.html.en, last access: 1 November 2023).

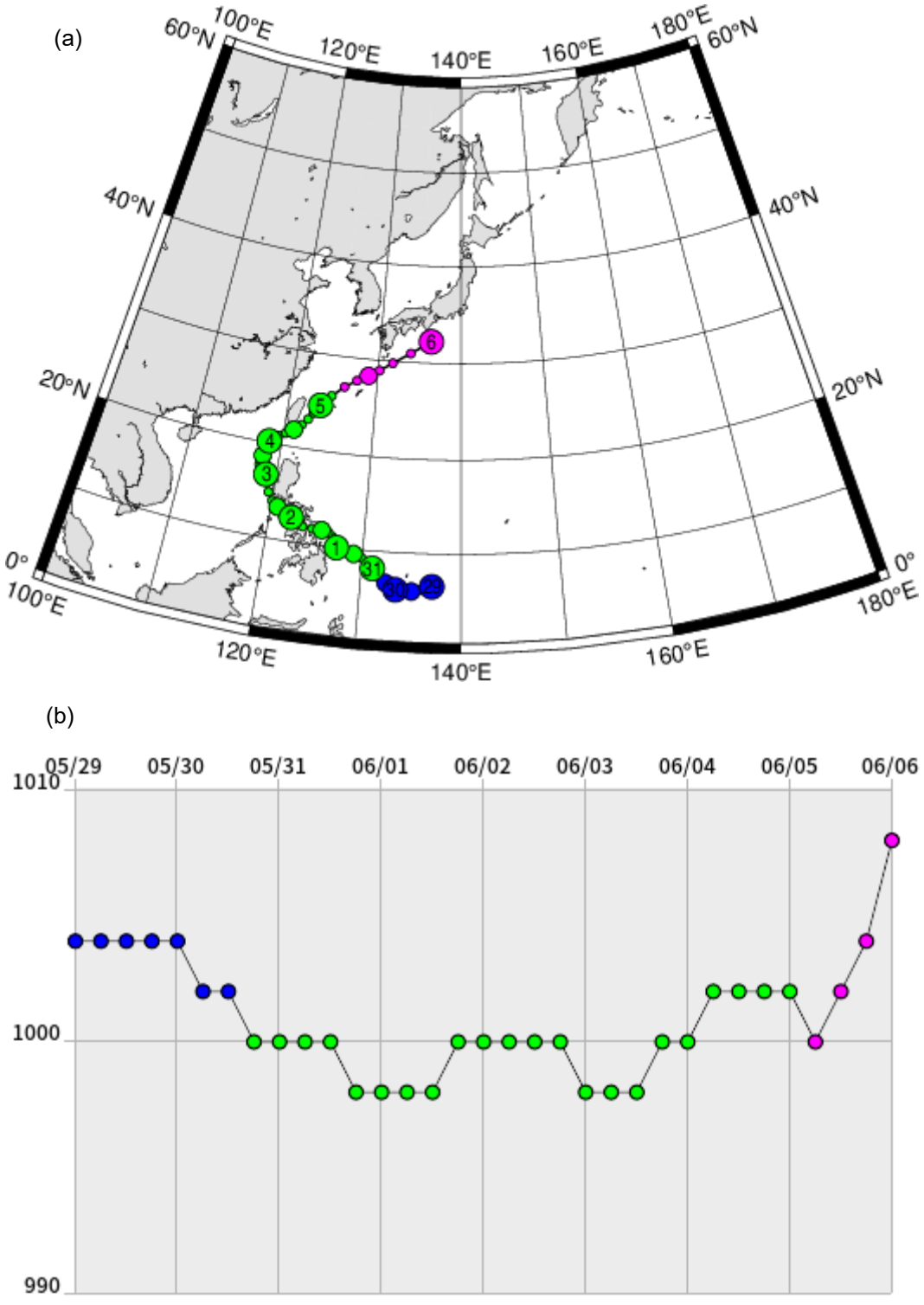

Fig. S5. (a) Best track map of the typhoon 202103 (CHOI-WAN), and **(b)** the central pressure chart (time zone=UTC, Local time=UTC+8).

S6. Multi-peak fitting of single particles

We didn't successfully obtain a bimodal or multi-peak fit for data of the stop cases using the multi-peak fitting function (LogNormal) in Igor Pro 8 software, as shown in Fig. S6, except Peak 0.

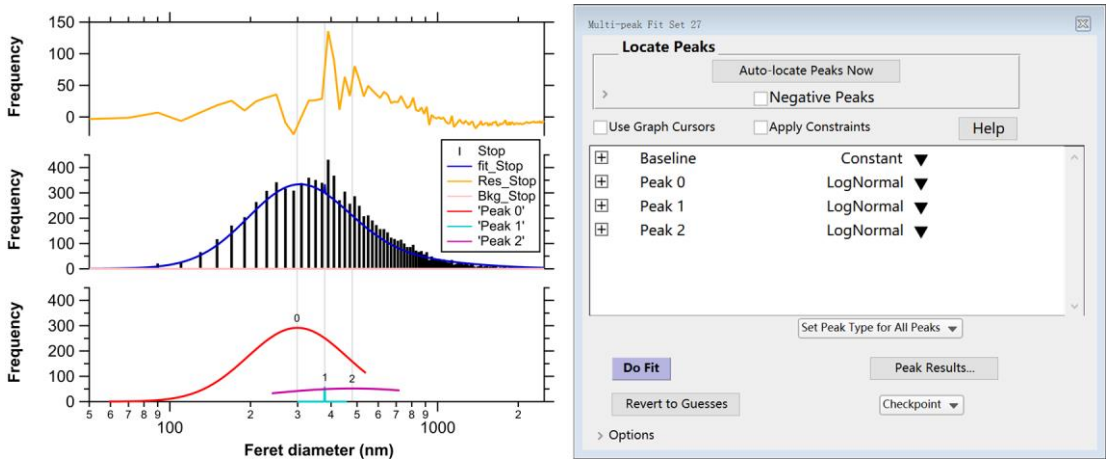

Fig. S6. Multi-peak fit particle size distribution using Feret diameter determined with Igor Pro 8 software during stop in **Fig. 5b** in the main text.

S7. TEM images and EDS spectrum of the BC particles and the tar balls

Figure S7 shows the TEM images of the three navigation samples before and after beam focus, revealing the presence of external and internal BC particles. Figure S8 presents the representative single particles and their corresponding EDS spectra for the navigation samples, indicating the major components are: (a, c) BC and sulfate, (b) sulfate, (d) sea salt, organics and BC. Notably, detecting nitrogen (N) element in EDS is challenging due to its high vaporization rate, whereas potassium (K) serves as a tracer for biomass burning in the BC- and sulfate-containing particles. The stop samples, shown in Fig. S9, exhibit both internal mixtures and externally large aggregates of the BC particles. The EDS point analysis of freshly emitted BC particles in Fig. S9c reveals the presence of very thin coating elements. In summary, the stop single particles were influenced by both ship's own emissions and long-range transport air masses. Figure S10 depicts example images of tar balls mixed with black carbon in the geometrical size range of 159–190 nm from the single particles collected during stop on 14 and 23 May. The backward trajectories suggest that the air masses originated from the Philippines, possibly due to biomass burning during those days. Figure S11 shows example images of pure BC particles, consisting of nano-soot particles with a diameter of 40–50 nm. The size of tar balls is larger than that of nano-soot spheres.

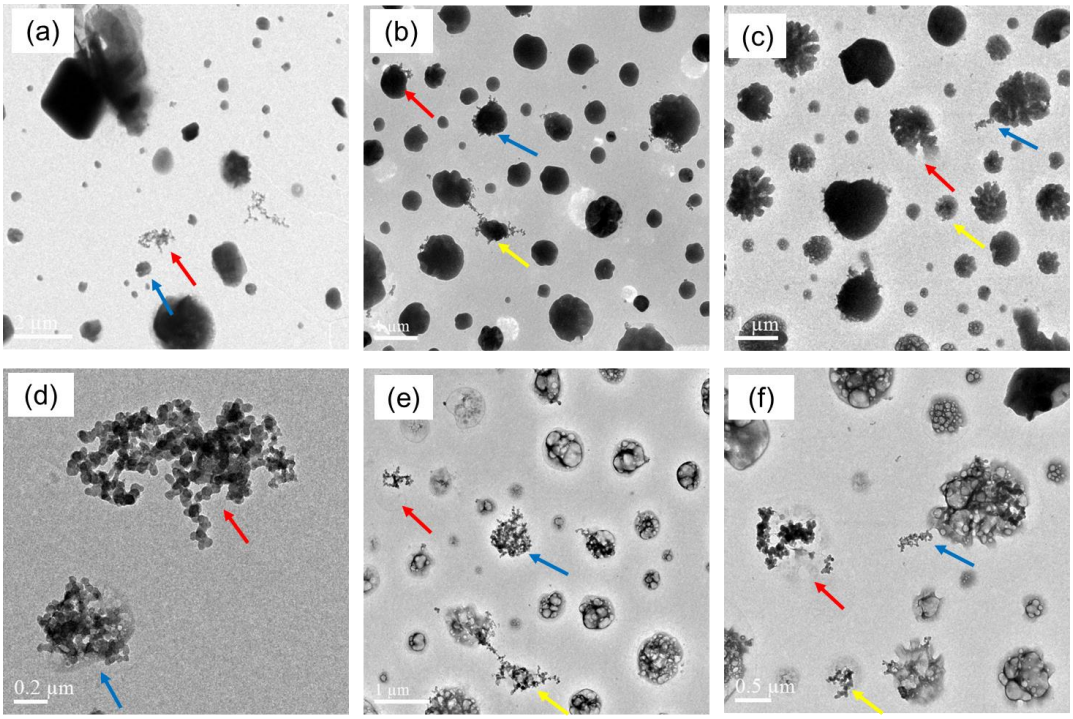

Fig. S7. The example TEM images before **(a, b, c)** and after **(d, e, f)** electron beam focus for the single particles collected during navigation. The same color arrows in each pair of images (**a** and **d**, **b** and **e**, **c** and **f**) indicate the same single particles.

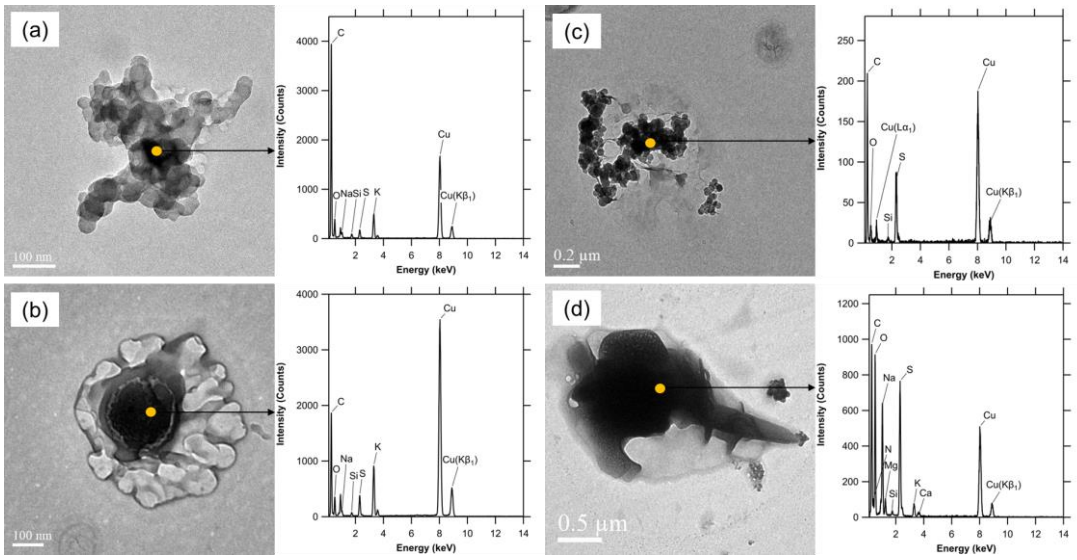

Fig. S8. Examples of the EDS spectra for the single particles from the navigation samples. Si and Cu are excluded from the particle composition. **(a)** BC, and thin sulfate coating (Na_2SO_4, K_2SO_4), **(b)** sulfate (Na_2SO_4, K_2SO_4), **(c)** BC, and thick sulfate coating, and **(d)** BC, sea salt. The orange spots indicate the point analysis of EDS spectra. The right spectrum corresponds to each left particle. The Y-axis is the intensity (counts) and X-axis is the energy (keV).

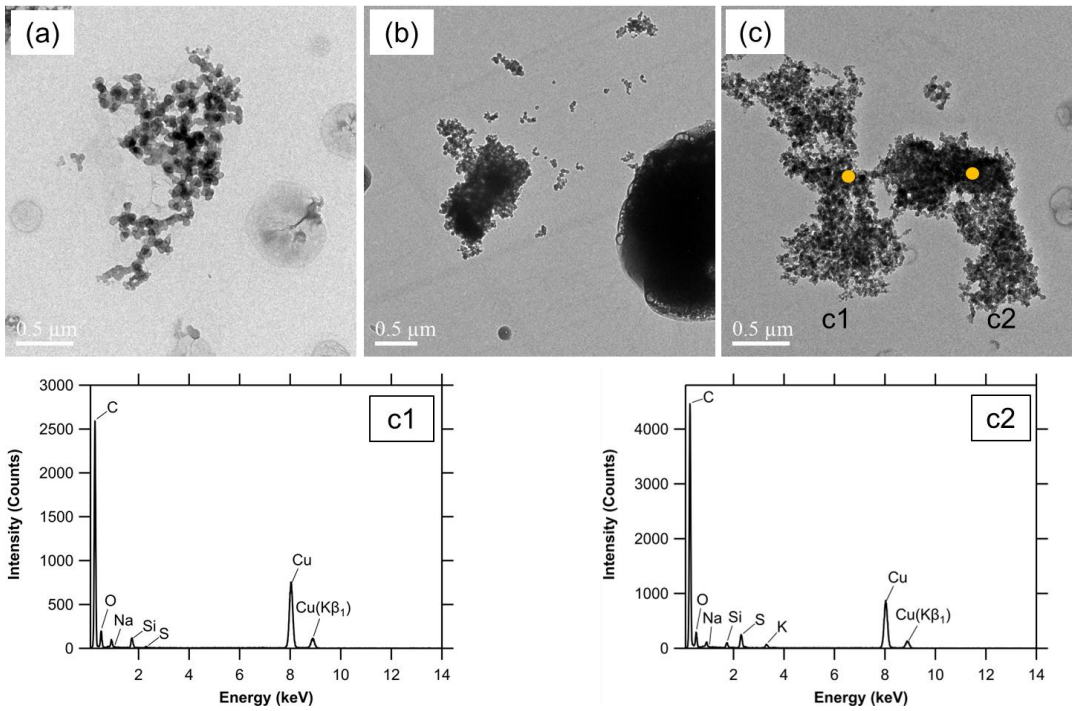

Fig. S9. The example TEM images **(a, b, c)** of BC particles collected during stop. The orange spots indicated point analysis of the EDS spectra (the left part **c1** and the right part **c2**) are for the image **(c)**.

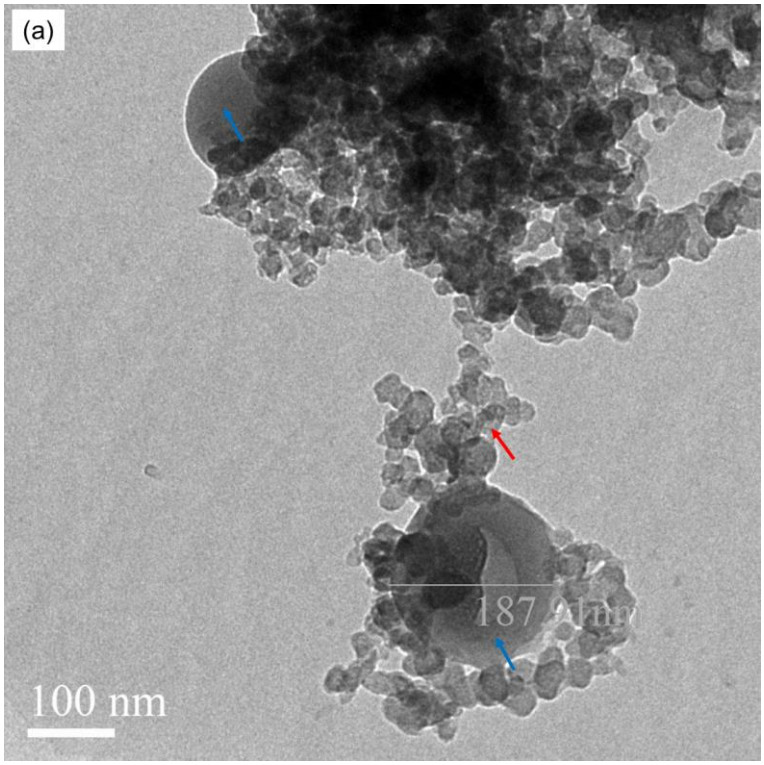

145

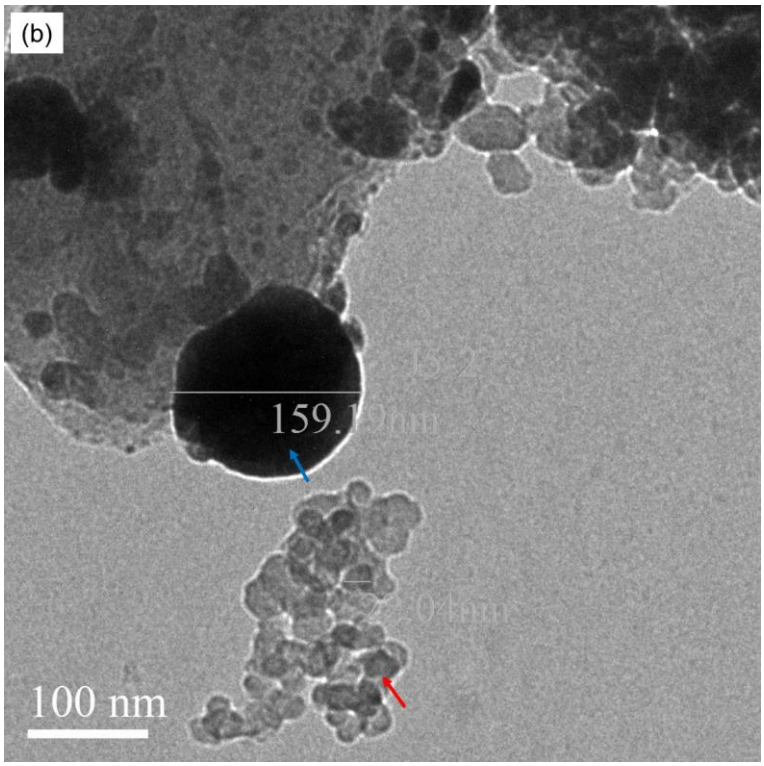

Fig. S10. Example images of tar ball-containing particles collected during stop: **(a)** tar balls (170–190 nm) mixed with black carbon (BC) and sea salt at 10:50:00 LT on 14 May 2021 and **(b)** tar balls consisting of 159 nm spherical particles at 08:39:00 LT on 23 May 2021. The red arrows indicated BC particles and the blue arrows indicated tar balls.

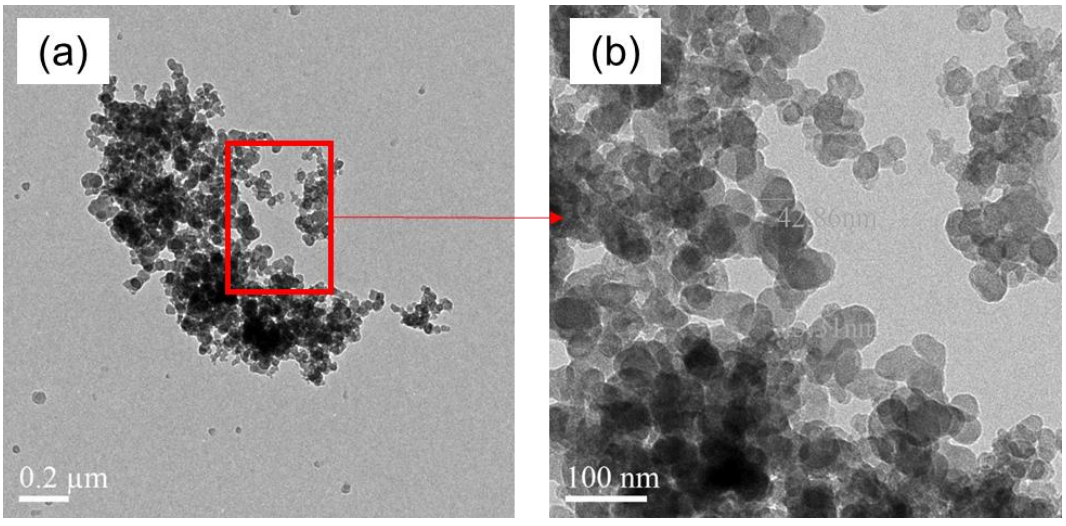

Fig. S11. Images of **(a)** aggregated BC particles, and **(b)** BC made of small 40–50 nm nano-soot spheres. The **S11(b)** image is a magnification of the part in the red rectangle in panel **a**.

S8. The diurnal average variation of OC, EC

Figure S12(a, b) shows the linear relationship between the Magee AE33 derived BC at 880 nm and the Sunset derived optical EC at 660 nm, with a time resolution of 1 min and 1h, respectively. The limit of detection (LOD) for optical EC, as determined by the Sunset OC/EC analyzer, is 0.062 μg m^{-3}, based on the blank filter analysis of three times the standard deviation (3σ). The fitted correlation between the two variables in Fig. S12a has a slope and intercept of the 0.97 and 0.44, respectively, with a determination coefficient (R^2) of 0.68. However, the linear correlation between the AE33 derived BC and the Sunset EC at a time resolution of 1 h has a slope and intercept of 1.66 and -0.01, respectively, with a higher R^2 of 0.91 (Fig. S12b). In addition, Fig. S12c displays the correlation between the optical EC and thermal EC data measured by the Sunset instrument. The slope and intercept of the fitted line are 1.55 and -0.21, respectively, with R^2=0.97. The differences of the two instruments are mainly attributed to the technical principles of the methods used for the data processing. Similar results have been reported in other studies (Brown et al., 2019).

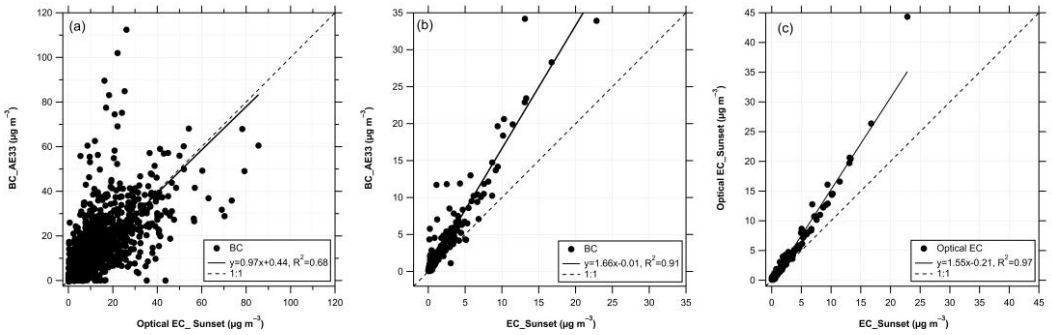

Fig. S12. The linear relationship between **(a)** the AE33 derived BC and the Sunset derived optical EC with a time resolution of 1 min, **(b)** thermal EC with a time resolution of 1 h, and **(c)** Sunset derived optical EC vs. thermal EC with a time resolution of 1 h for all the data during the campaign in the SCS.

S9. Possible biological particles collected during the campaign

Two examples of possible biological particles were collected on two different days. Figure S13a displays brochosomes, which are known to be produced by leaf-hopping insects. This finding is supported by a previous study (Fu et al., 2012). Figure S13b depicts a rod-like particle that has yet to be identified.

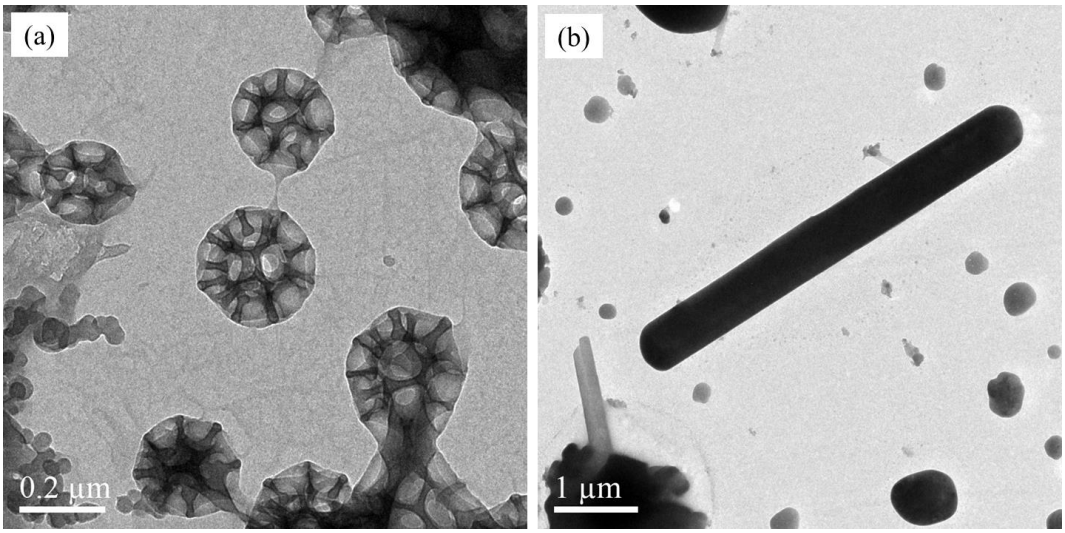

Fig. S13. (a) Flower-like biological particles collected at 10:50:00 LT on 14 May 2021, and **(b)** rod-like biological particles collected at 08:01:00 LT on May 24, 2021.

S10. CALIPSO observation

Cloud-Aerosol Lidar & Infrared Satellite Observation (CALIPSO) is a remote sensor on board the TERRA and AQUA satellites. CALIPSO observation can provide vertical and horizontal distribution of the cloud and aerosol layers using the elastic backscatter intensities (extinction-to-backscatter ratio) at an Nd:YAG laser wavelength of 532 and 1064 nm near the nadir of the orbit track. CALIPSO L1 Standard V4.20 products are available from the NASA Langley Research Center (https://www-calipso.larc.nasa.gov/tools/data_avail/, last access: 31 March 2023). Images of vertical feature mask (VFM) and aerosol subtype (AS) were used to show the vertical and horizontal properties of clouds, aerosol layer and identification (Liu et al., 2019; Omar et al., 2009). Convective transport is important to the vertical distribution of aerosols (Niu et al., 2019).

Figures S14 and S15 show the orbit track location, vertical feature mask, and aerosol subtype at 06:00:00 on 15 May 2021, and at 19:30:00 on 7 June 2021, respectively. These images show that polluted continental, smoke and elevated smoke exist in the aerosol layer with an altitude of 1–3 km over the SCS regions and Southeast Asia.

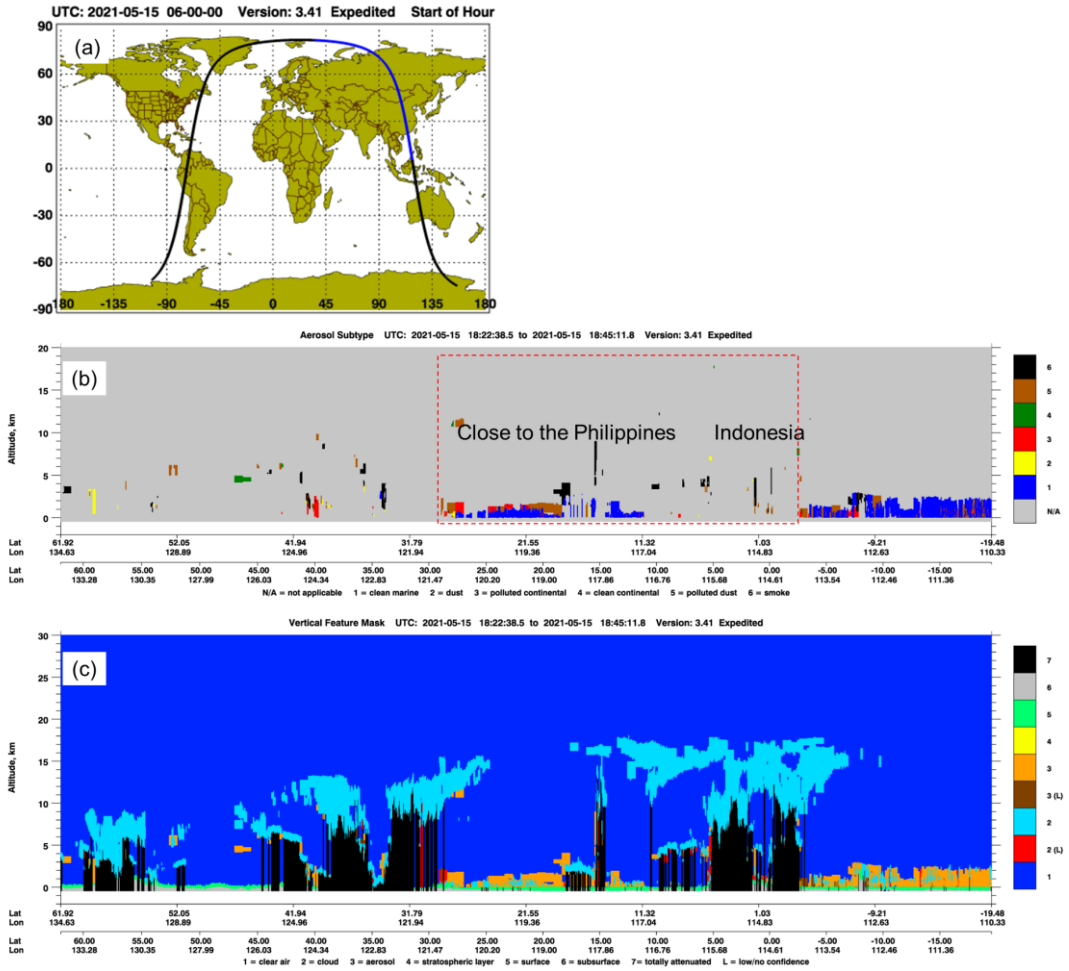

Fig. S14. (a) Orbit track location indicated by blue curve, **(b)** vertical feature mask, and **(c)** aerosol subtype at 06:00:00 UTC on 15 May 2021, a time before the summer monsoon started in the SCS.

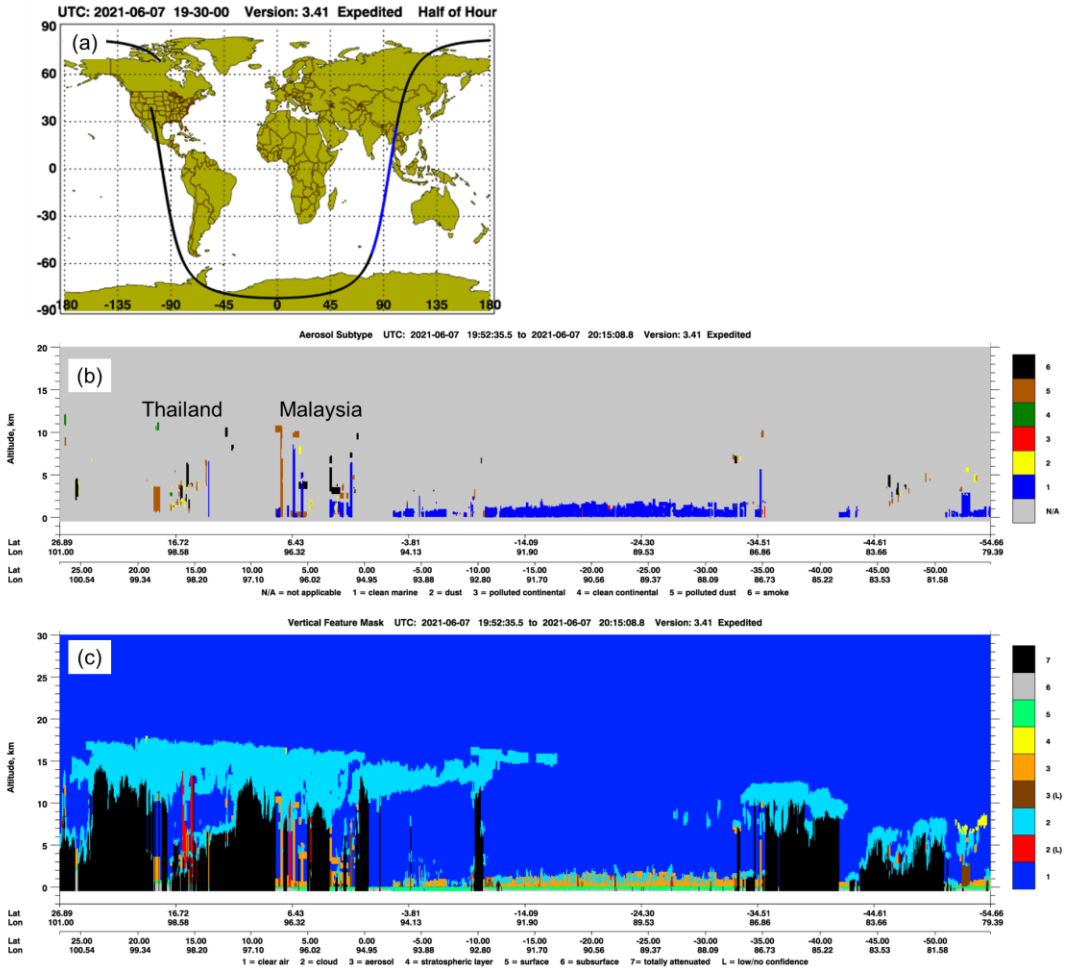

Fig. S15. (a) Orbit track location indicated by blue curve, **(b)** vertical feature mask, and **(c)** aerosol subtype at 19:30:00 UTC on 7 June 2021, a time after summer monsoon passed in the SCS.

S11. Time resolution and accuracy for the automatic weather station

The time resolutions for the original meteorological and GPS data are 3 s. The position accuracies for the X and Y axes are 1 cm +1 ppm RMS (root mean square), and for Z axis is 2 cm +1 ppm RMS. The accuracy of wind speed and wind direction is ± 0.2 m s^{-1} (or 3% of reading) and ± 2°, respectively. The accuracy of temperature with RS-485 output at +20 to +60 °C is ± (0.07 + 0.0025 × temperature) °C. The accuracy of relative humidity at -20 to + 40 °C is ± (1 + 0.008 ×reading) %RH. The accuracy of pressure with factory calibration is ± 0.15 hPa (Class A).

S12. Additional BC fractal analysis

A combination of BC particles in this study collected in the South China Sea and previous BC particles collected on an island in the East China Sea (Sun et al, 2020) is shown in Fig. S16.

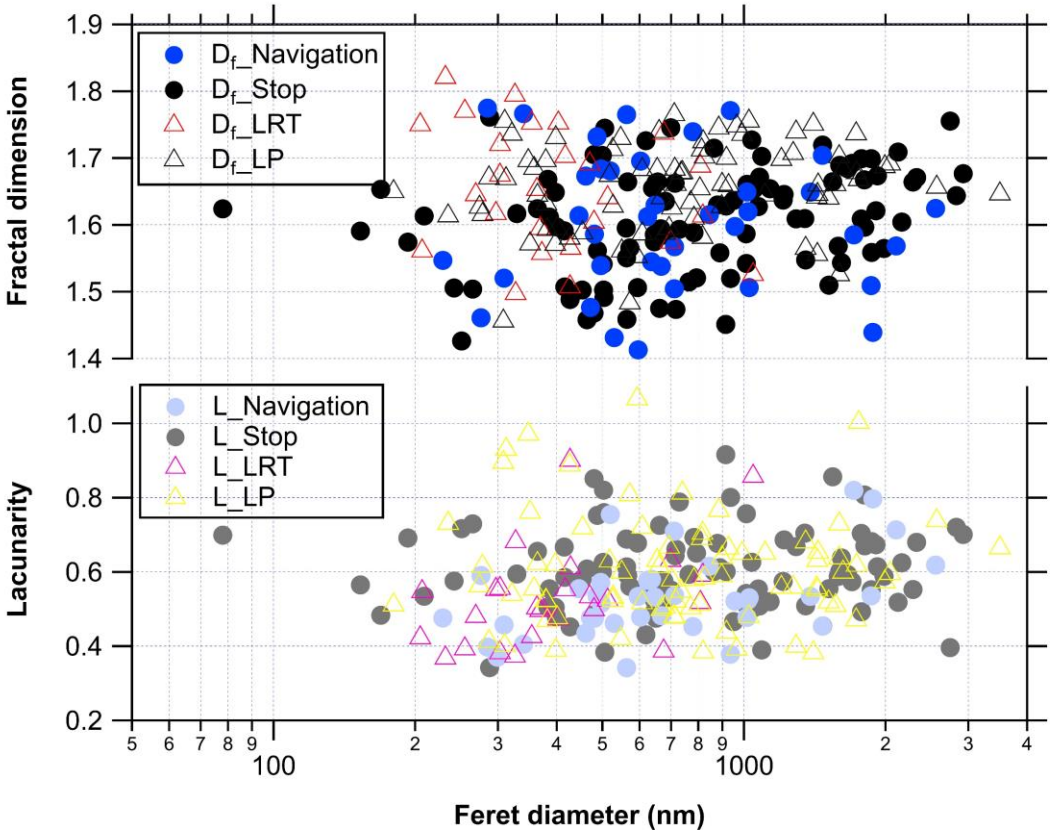

Fig. S16. The size-dependent fractal dimension (D_f) and lacunarity (L) for each BC particle during navigation and stop. A total number of 240 data points are shown in Fig. S16. LRT and LP indicated particles from long-range transport and local pollution, respectively.

References

Brown, S., Minor, H., O'Brien, T., Hameed, Y., Feenstra, B., Kuebler, D., Wetherell, W., Day, R., Tun, R., Landis, E., and Rice, J.: Review of Sunset OC/EC instrument measurements during the EPA's Sunset carbon evaluation project, Atmosphere (Basel), 10, 287, https://doi.org/10.3390/atmos10050287, 2019.

Fu, H., Zhang, M., Li, W., Chen, J., Wang, L., Quan, X., and Wang, W.: Morphology, composition and mixing state of individual carbonaceous aerosol in urban Shanghai, Atmos. Chem. Phys., 12, 693–707, https://doi.org/10.5194/acp-12-693-2012, 2012.

Liu, Y., Zhu, Q., Wang, R., Xiao, K., and Cha, P.: Distribution, source and transport of the aerosols over Central Asia, Atmos. Environ., 210, 120–131, https://doi.org/10.1016/j.atmosenv.2019.04.052, 2019.

Marple, V. A. and Olson, B. A.: Sampling and measurement using inertial, gravitational, centrifugal, and thermal techniques, in: Aerosol measurement: Principles, techniques, and applications, edited by: Kulkarni, P., Baron, P. A., and Willeke, K., John Wiley and Sons, Hoboken, New Jersey, USA, 129–151, https://doi.org/10.1002/9781118001684.ch8, 2011.

Niu, H., Kang, S., Gao, W., Wang, Y., and Paudyal, R.: Vertical distribution of the Asian tropopause aerosols detected by CALIPSO, Environ. Pollut., 253, 207–220, https://doi.org/10.1016/j.envpol.2019.06.111, 2019.

Omar, A. H., Winker, D. M., Vaughan, M. A., Hu, Y., Trepte, C. R., Ferrare, R. A., Lee, K.-P., Hostetler, C. A., Kittaka, C., Rogers, R. R., Kuehn, R. E., and Liu, Z.: The CALIPSO automated aerosol classification and Lidar ratio selection algorithm, J. Atmos. Ocean. Technol., 26, 1994–2014, https://doi.org/10.1175/2009jtecha1231.1, 2009.

Sorensen, C. M. and Roberts, G. C.: The prefactor of fractal aggregates, J. Colloid. Interf. Sci., 186, 447–452, https://doi.org/10.1006/jcis.1996.4664, 1997.

Sun, C., Adachi, K., Misawa, K., Cheung, H. C., Chou, C. C. K., and Takegawa, N.: Mixing state of black carbon particles in Asian outflow observed at a remote site in Taiwan in the spring of 2017, J. Geophys. Res. Atmos., 125, e2020JD032526, https://doi.org/10.1029/2020jd032526, 2020.

Sun, C., Zhang, Y., Liang, B., Gao, M., Sun, X., Li, F., Ni, X., Sun, Q., Ou, H., Chen, D., Zhou, S., & Zhao, J.: Comprehensive data on meteorology, black carbon, organic carbon, elemental carbon, and aerosol morphology from the South China Sea summer expedition in 2021 [Data set], Zenodo, https://doi.org/10.5281/zenodo.10546755, 2024.

Zhang, K., Allen, G., Yang, B., Chen, G., Gu, J., Schwab, J. J., Felton, D., and Rattigan, O.: Joint measurements of $PM_{2.5}$ and light-absorptive PM in woodsmoke-dominated ambient and plume environments, Atmos. Chem. Phys., 17, 11441–11452, https://doi.org/10.5194/acp-17-11441-2017, 2017.